Generic Contrast Agents
Our portfolio is growing to serve you better. Now you have a *choice*.
FRESENIUS KABI
VIEW CATALOG

AJNR

Multivoxel proton MR spectroscopy and hemodynamic MR imaging of childhood brain tumors: preliminary observations.

A A Tzika, S Vajapeyam and P D Barnes

AJNR Am J Neuroradiol 1997, 18 (2) 203-218
http://www.ajnr.org/content/18/2/203

This information is current as of May 8, 2025.

Multivoxel Proton MR Spectroscopy and Hemodynamic MR Imaging of Childhood Brain Tumors: Preliminary Observations

A. Aria Tzika, Sridhar Vajapeyam, and Patrick D. Barnes

PURPOSE: To assess multivoxel proton MR spectroscopy combined with MR imaging and hemodynamic MR imaging in the evaluation of brain tumors in children and young adults. **METHODS:** Fifteen patients with brain tumors and 10 healthy children underwent MR imaging and MR spectroscopy on a 1.5-T system. Ten patients with tumors had both MR spectroscopy and hemodynamic MR imaging. MR spectroscopy data sets with 1 cm^3 to 3.4 cm^3 resolution were acquired within 8.5 minutes by using a point-resolved spectroscopic, chemical-shift imaging technique in two dimensions with volume preselection. MR imaging was performed using fast spin-echo techniques. Hemodynamic MR imaging data were acquired every 2.5 seconds at one anatomic level using a spoiled gradient-echo sequence during intravenous bolus administration of contrast material. **RESULTS**: Assessment with multivoxel MR spectroscopy and hemodynamic MR imaging added about 30 minutes to the total MR examination time. Normal tissue exhibited spectral peaks from biologically significant compounds such as *N*-acetylaspartate (NAA), choline-containing compounds (Cho), and total creatine (tCr). Twelve biopsy-proved tumors exhibited prominent Cho, reduced NAA, variable tCr, and/or lactate or lipids, and two showed increased hemodynamic parameters. Three of the tumors treated with radiation did not reveal prominent levels of Cho. Tissue necrosis had no Cho, NAA, or tCr, and reduced hemodynamics. **CONCLUSIONS:** Preliminary findings by MR spectroscopy combined with MR imaging and hemodynamic MR imaging suggest that regions of active tumor may be differentiated from areas of normal tissue and areas of necrosis. These findings may enable metabolic and hemodynamic characterization of childhood brain tumors as well as suggest their response to therapy.

Index terms: Brain neoplasms, magnetic resonance; Children, neoplasms; Magnetic resonance, spectroscopy

AJNR Am J Neuroradiol 18:203–218, February 1997

Control of brain tumors remains a significant problem in children (1). The current study was designed because both computed tomography (CT) and magnetic resonance (MR) imaging are frequently unable to distinguish between therapy-related tissue reaction and progression or recurrence of tumor growth. At present, the standard method for making this distinction is histology. Positron emission tomography (PET) and single-photon emission CT (SPECT) are currently the only techniques that provide functional imaging information (2, 3), but they use ionizing radiation and are expensive. Recent advances have permitted the use of proton MR spectroscopy and hemodynamic MR imaging in the clinical setting (4–6). If performed at regular intervals during treatment, both techniques have great promise for predicting and monitoring treatment effectiveness.

MR spectroscopy can assess the spatial distribution of selected brain metabolites by using multivoxel, chemical-shift imaging techniques (7–15). Chemical-shift imaging provides simultaneous spectra from multiple contiguous voxels, thus providing metabolic information from

Received December 11, 1995; accepted after revision July 30, 1996.

Recipient of the Derek C. Harwood-Nash award at the annual meeting of the American Society of Pediatric Neuroradiology, Chicago, Ill, April 1995.

From the Department of Radiology, Children's Hospital and Harvard Medical School, Boston, Mass (A.A.T., S.V., P.D.B.); and the Magnetic Resonance Science Center, University of California at San Francisco (A.A.T.).

Address reprint requests to A. Aria Tzika, PhD, Department of Radiology, Children's Hospital, 300 Longwood Ave, Boston, MA 02115.

AJNR 18:203–218, Feb 1997 0195-6108/97/1802–0203

© American Society of Neuroradiology

more than one region of interest. Observing the effect of paramagnetic agents on the magnetic susceptibility of tissue signal intensity (16, 17) and monitoring the transit of intravascular or diffusible tracers through the brain have been done to assess regional hemodynamics (4, 5, 18) (B. R. Rosen, J. W. Belliveau, D. Chien, M. S. Cohen, R. M. Weisskoff, "MR Perfusion Imaging," In: H. Y. Dressel, M. T. Modic, W. A. Murphy, eds, *Syllabus: Special Course 'MR 1990,* Oak Brook, Ill: Radiological Society of North America; 1990:69–84).

The pathophysiology of brain tumors includes changes in both cellular and hemodynamic events. MR spectroscopy provides biochemical information of pathophysiological changes at the cellular level. Hemodynamic MR imaging reflects the hemodynamic state of the tissue, which is potentially altered by neoplasia due to neovascularity. The additional information provided by these techniques is independent of each other but complementary to MR imaging.

In the present work we tested the hypothesis that the use of MR spectroscopy combined with MR imaging and hemodynamic MR imaging to examine pediatric patients undergoing treatment for brain tumors has the potential to distinguish tumor growth or tumor recurrence from normal tissue and necrosis. We applied these methods in children and young adults with preoperative and postoperative brain tumors.

Subjects and Methods

Subjects

Fifteen patients with brain tumors (five female and 10 male, 19 months to 24 years old) (Table 1), and 10 healthy children (six girls and four boys, 3 months to 15 years old), were examined on a 1.5-T whole-body MR imaging system equipped with a quadrature head coil. Informed consent was obtained from the parents of all subjects. Fifteen MR imaging examinations, 15 MR spectroscopy examinations, and 10 hemodynamic MR imaging examinations of the patients with brain tumors were performed. One hemodynamic MR imaging examination was inconclusive owing to movement (patient 8, Table 1). The MR spectroscopy/hemodynamic MR imaging findings of these patients were analyzed and compared with histologic findings. They were not compared with conventional MR imaging findings, since that information is outside the scope of this study.

MR Protocol

The MR protocol included conventional MR imaging, proton MR spectroscopy, hemodynamic MR imaging ($T2^*$-weighted spoiled gradient-echo imaging), and volume T1-weighted spoiled gradient-echo imaging. Only patients with tumors had both MR spectroscopy and hemodynamic MR imaging.

Conventional MR imaging was performed using spin-echo sagittal T1-weighted sequences (600/20/2 [repetition time/echo time/excitations], 24-cm field of view [FOV], 5-mm section thickness with a 20% intersection gap, and a 128 × 256 acquisition matrix); fast spin-echo (FSE) proton density–weighted sequences (2000/17 effective/1, 24-cm FOV, 5-mm section thickness with a 50% intersection gap, a 192 × 256 matrix, and an echo train length [ETL] of 4); and FSE T2-weighted sequences (3200/85 effective/1, 24-cm FOV, 5-mm section thickness with a 50% intersection gap, a 192 × 256 matrix, and an ETL of 8). The volume MR imaging protocol for segmentation purposes included proton density–weighted FSE sequences (2000/17, ETL of 4) and T2-weighted FSE sequences (3200/85, ETL of 8) with 3-mm interleaved contiguous multisection images and a 24-cm FOV.

Proton MR Spectroscopy Technique

Proton MR spectroscopy (two-dimensional chemical-shift imaging) was performed by using point-resolved spectroscopy (19) (P. A. Bottomley, "Selective Volume Method for Performing Localized NMR Spectroscopy," US patent 1984;4 480 228). After selecting a 50- to 100-cm^3 volume and making shimming and water-suppression adjustments, one spectrum was first collected from the entire volume and then a large data set was obtained using phase-encoding gradients in two directions (two-dimensional chemical-shift imaging). The following parameters were used: 1000/65/2, 16 × 16 phase-encoding matrix, 160-mm FOV, 10-mm section thickness, 1250-Hz spectral width, and 512 points. Data sets of 1.0- to 3.4-cm^3 resolution were acquired within 8.5 minutes. Data processing was performed on a Sunsparc 10 workstation (Sun Microsystems, Mountain View, Calif) using analysis software developed by Sarah J. Nelson (Department of Radiology, Magnetic Resonance Science Center, University of California San Francisco). The data sets were apodized with a 1.0-Hz lorentzian filter, Fourier-transformed in the time domain and the two spatial domains, and phased. Voxel position was shifted using the voxel shifting capability of the Fourier transform to obtain spectra from specific locations on the MR images. Modifications of the Piqable algorithm were used for peak analysis (20). Segmentation and generation of metabolite images were done by using General Electric research workstation software.

Spectral quantification was performed using the Piqable algorithm (20). The spectra were first manually phased using Sage, and then the areas of selected metabolite peaks such as choline-containing compounds (Cho), total creatine (tCr), *N*-acetylaspartate (NAA), and lactate/lipids

were estimated using Piqable (Table 2). Since the area under the tCr peak is relatively constant throughout normal brain tissue, its mean value has been used as an internal standard or reference peak (R) to estimate relative changes of the other metabolites. Each patient served as his or her own control subject. Several spectra were used to derive the mean values for Cho, tCr, NAA, and lactate/lipid peak areas within tumor or normal regions. The normal regions were selected from a contralateral area or an area adjacent to the tumor site.

A locally linear baseline estimator was used to subtract the broad components of the baseline before making peak area calculations. Metabolite images were also generated using Sage, stored as TIFF files on the Sunsparc workstation, and then transferred to a Macintosh Quadra 950 over the Ethernet. Conventional MR images and the spectral data were also transferred to the Macintosh. The image and spectral data were then processed using NIH Image, Adobe Photoshop, and Powerpoint software.

Hemodynamic MR Imaging

Hemodynamic MR imaging was performed using a spoiled gradient-echo sequence during an intravenous bolus injection of 0.1 mmol/kg gadopentetate dimeglumine within 3 to 5 seconds (21). The following parameters were used: 24/15/0.75, flip angle of 10°, 26-cm FOV, 10-mm section thickness, and 128 × 256 acquisition matrix. Images were acquired every 2.5 seconds at one anatomic level as selected from the MR images. Data analysis was performed by means of a program written in "C" that generated hemodynamic parameter maps (W-C. Liu, R. Massoth, A. Tzika, R. Dunn, W. Ball, "Automation for MRI-Derived Hemodynamic Parameter Analysis," in: *Proceedings of the Society of Magnetic Resonance in Medicine*, Berkeley, Calif: Society of Magnetic Resonance in Medicine; 1993:714).

The procedure for calculating the hemodynamic parameters is as follows: an average precontrast signal intensity (SI_0) is calculated; a noise threshold value, obtained from the known noise level of the MR scanner, is used to generate a mask image to suppress background noise; the concentration or $\Delta R2^*(t)$ matrix is then calculated on a pixel-by-pixel basis, where $R2^* = 1/T2^*$, $\Delta R2^*(t) = \ln [SI_0/SI(t)]/TE$, and SI(t) is the signal intensity at time (t). The average section value of $\Delta R2^*$ versus time is plotted by using a cubic spline fit. The area under the $\Delta R2^*$ peak is numerically integrated. Percent signal intensity images and various parameter images are then calculated. The program generates a series of signal intensity images that show the intensity distribution across the selected section as a percentage of the average precontrast intensity distribution, calculated on a pixel-by-pixel basis for each image. The hemodynamic parameter maps of interest that are generated include the relative cerebral blood volume (rCBV) map, which is the area under the $\Delta R2^*$ peak calculated by pixelwise numerical integration; the mean transit time (MTT) map, calculated from the effective width of the $\Delta R2^*$ curve; and the cerebral blood flow (rCBF) map, which is the ratio of the area under the $\Delta R2^*$ (t) curve to the difference between the MTT and the mean bolus injection time, calculated on a pixelwise basis.

Statistical Analysis

Statistical analysis of the metabolite ratios was performed using Systat 5.2.1 (Systat, Inc, Evanston, Ill). A paired variable *t* test was performed to evaluate differences in metabolite ratios between normal and tumor regions in patients, and an independent variable *t* test was used to compare metabolite ratios in normal regions of the brain in patients with the corresponding ratios in control subjects. Differences between the means were considered significant if the *P* values were beyond the .05 level of confidence.

Results

High-quality data were obtained for healthy control subjects using the MR spectroscopy protocol described above. Three prominent peaks were detected with a high signal-to-noise ratio: NAA (10.7 ± 3.5), tCr (8.8 ± 2.8), and Cho (8.6 ± 3.5). The metabolite ratios of interest in this study, namely NAA/R and Cho/R, also showed 9.8% and 19.3% intersubject variability (defined as standard deviation/mean expressed as a percentage), respectively. With our protocol, we were able to acquire high-quality data sets of up to 1 cm^3 resolution reproducibly in the patients with tumors, and show abnormal metabolite levels even in small tumors. In most cases, the three most prominent metabolite peaks were distinguished from one another. In some cases lactate and/or lipid was also present.

Table 1 summarizes the MR imaging and histologic findings from 15 children and young adults with brain tumors. Patients 1 through 4 (with pilocytic astrocytoma, cerebral anaplastic ependymoma, cerebellar anaplastic ependymoma, and malignant glial neoplasm, respectively) were studied before surgical and/or radiation treatment and the findings were reviewed within the context of the histologic findings on specimens obtained at surgery (Table 1). Patients 5 through 8 (with fibrillary astrocytoma, fibrillary glial neoplasm, infiltrative glial neoplasm, and cellular ependymoma, respectively) were studied after surgical treatment. Patients 9 through 13 (with cerebral anaplastic astrocytoma, cerebral anaplastic ependymoma, astrocytic ependymoma, poorly differentiated neuroepithelial tumor, and cerebral glioblastoma

TABLE 1: Findings at MR imaging, hemodynamic MR imaging, surgery, and histologic examination in 15 children and young adults with brain tumors

Patient	Age, y/Sex	MR and Surgical Findings	Histologic Findings
1	7/M	L hemisphere thalamic mass: 60%–70% of lesion was solid, characterized by heterogeneous enhancement; 30%–40% was cystic. Hemodynamic MR imaging showed low hemodynamics.	Pilocytic astrocytoma.
2	5/F	Large heterogeneous mass within the R parietal and frontal lobes; solid components were posterior, large cystic component was anterior; heavy calcification of the solid component; surrounding edema; R lateral ventricle was effaced; ringlike enhancement within the more solid portion of the lesion.	Anaplastic ependymoma: the tumor consists of sheets and clusters of cells showing considerable pleomorphism. Abundant mitosis, fibrillary background, and some areas of well-developed pseudorosettes. Vascular endothelial proliferation and microscopic foci of necrosis throughout the tumor. Immunostaining for proliferation marker shows strong positivity. Although some tumor regions are well-differentiated ependymoma, there are regions of poorly differentiated ependymoma with brisk mitotic index, high proliferation index, and vascular proliferation. Ultrastructural features expected in tumors with ependymal differentiation.
3	4/M	Large, mixed signal, midline, fourth ventricular mass showed mild enhancement. Areas of very low, nonenhancing regions consistent with necrosis and/or cyst; slight mass enhancement with no meningeal or subependymal enhancement to suggest seeding. Hemodynamic MR imaging showed areas of higher and lower hemodynamics.	Anaplastic ependymoma: cellular tumor exhibiting two histologic patterns, present in approximately equal amounts; dense cellular areas with moderate perivascular pseudorosettes, extensive areas of confluent as well as single-cell necrosis, and prominent endothelial proliferation with numerous mitotic figures; other areas are less cellular with perivascular pseudorosettes and rare true rosettes with fibrillary background, less apparent necrosis and endothelial proliferation.
4	15/M	History of hepatoblastoma treated with chemotherapy 10 y prior; now with left frontoparietal enhancing tumor involving leptomeninges, motor cortex.	Malignant glial tumor: densely cellular tumor without architectural or cytologic differentiation; mitosis and foci of necrosis; other portions of specimen represent cerebral cortex with extensive infiltration of highly aggressive tumor.
5	10/M	Postoperative evaluation of brain stem glioma extending into the suprasellar region. Large intraaxial mass involving pons, midbrain, and thalami. Isointense T1 weighting, increased T2 weighting, and diffuse contrast enhancement.	Fibrillary astrocytoma with piloid features in association with abundant eosinophilic bodies and Rosenthal fibers.
6	22/M	Previous resection 5 y earlier of a mass with similar appearance at biopsy. R thalamic enhancing lesion; enhancement similar to previous examination 6 months ago; cystic component increased in size; more mass effect on R lateral ventricle and minimal midline shift at the level of the thalami; stable R parietal postsurgical changes. Hemodynamic MR imaging exhibited low hemodynamics after stereotactic radiation therapy.	Recurrent fibrillary glial neoplasm with Rosenthal fibers: focal endothelial proliferation; no mitotic figures, necrosis or pleomorphism.
7	17/M	Resection performed 4 y ago. Brain stem lesion with heterogeneous peripheral and some central enhancement with focus of hemorrhage on the superior aspect of mass. Brain stem glioma; heterogeneous signal intensity. Hemodynamic MR imaging showed hemodynamics lower than gray matter.	Diffusely infiltrative glial neoplasm without anaplastic features.
8	17/M	Postoperative L frontal lobe changes. Surgical cavity with some heterogeneous peripheral regions of enhancement. Punctate foci of mineralization. Stable high T2 signal surrounding the surgical cavity.	Cellular ependymoma with necrosis and hemorrhage: extensive areas of well-defined ependymal perivascular pseudorosettes.

Table continues.

TABLE 1: Continued

Patient	Age, y/Sex	MR and Surgical Findings	Histologic Findings
9	24/M	Examination after resection and radiation therapy; a L parietooccipital cystic mass was resected 1 year ago. Surgical defect in the L parietal lobe; increased T2 signal anterior to the defect, which may exert some mass effect on the ventricle; residual tumor cannot be excluded from this region; no significant enhancement.	Biopsy samples at surgery revealed an anaplastic astrocytoma; prominent pleomorphism; infiltrating cortex posteriorly.
10	18/F	Examination after surgery and radiation therapy. Multiple recurrence of a L temporal lobe tumor; first resection 2 y prior. Interval increase in the cystic lesion with rim enhancement; mild peritumoral edema characterized by increased T2 signal; interval increase in the mass effect on the L lateral ventricle with L-to-R midline shift; enhancement in the medial aspect of the L temporal lobe at the junction with the lower L frontal lobe. Hemodynamic MR imaging exhibited early enhancement consistent with high vascular permeability.	Recurrent anaplastic ependymoma: highly cellular neoplasm with mitosis; poorly differentiated tumor with glial features; areas of ependymal differentiation in the form of perivascular pseudorosettes; mitoses are abundant; regional necrosis, granulation tissue, and vascular changes with numerous thin-walled vessels both within tumor and hyalinized fibrous tissue; these may be related to effects of prior treatment; more ependymal differentiation than previously; more necrosis and higher mitotic rate.
11	8/F	Follow-up of posterior fossa/supratentorial mass after radiation. Extensive signal abnormality involving both cerebellar hemispheres, R dorsal pons, the R midbrain, and the thalamus. Hemodynamic MR imaging exhibited early enhancement of mass, particularly of the rim.	Glioma of moderate cellularity. Both astrocytic and ependymal features. Rare foci of necrosis and scattered foci of calcification. No mitotic figures. Reactive tissue features consistent with surgery and radiation changes.
12	6/F	Poorly differentiated tumor resected 1 y prior followed by standard radiation therapy and radiosurgery; ring enhancement is seen around surgical site; radiation necrosis or recurrent tumor? Hemodynamic MR imaging showed diminished hemodynamics at that site.	Dense collagenous scar with extensive gliosis and macrophage infiltration in white matter and cerebral cortex consistent with treatment effect; no tumor is identified.
13	14/M	Examination after resection and radiation therapy; R temporoparietal and occipital cystic area with increased T2 signal in the posterior limb of internal capsule. Hemodynamic MR imaging exhibited early enhancement consistent with high vascular permeability.	Posterior lesion shows focal necrosis gray and white matter reactive changes and small focus of glioma. The cyst wall shows hypercellularity, thickened blood vessels, and focal regions containing scattered macrophages, all of which are consistent with treated residual malignant glioma.
14	15/M	Eight weeks into chemotherapy; originally diagnosed 2 y prior. Midline enhancing mass involving the hypothalamus and suprasellar cistern with extension into the third ventricle. No significant change from previous follow up 1 month ago and no new lesions. Hemodynamic MR imaging showed that the hemodynamics of anterior portion of the mass was higher than white matter, although the posterior did not differ from white matter.	Recurrent medulloblastoma.
15	1/F	Postchemotherapy evaluation. R frontal lesion without contrast enhancement.	Infiltrating glioma.

multiforme, respectively) were studied after surgical and radiation treatment (Table 1). Patients 14 and 15 (with medulloblastoma and supratentorial glioma, respectively) were studied after chemotherapy. Table 2 summarizes the quantitative MR spectroscopy findings and gives the values of metabolite levels and selected metabolite ratios. The mean values and standard deviations of Cho_n/R and NAA_n/R were 0.93 ± 0.19 and 1.51 ± 0.38, respectively. The difference between these mean values and the ones from healthy control subjects (Cho_n/R, 0.88 ± 0.17; NAA_n/R, 1.74 ± 0.17) is not significant ($P = .48$ and $P = .09$).

In patients 1 through 10, 14 to 15 regions of biopsy-proved tumor exhibited prominent Cho, reduced NAA, and variable tCr levels (Figs 1–4). Peaks consistent with methyl or methylene groups arising from free lipids or lactic acid were identified in patients 2, 3, 10, 11, 14, and

TABLE 2: Quantitative MR spectroscopic findings and tumor grade in 15 patients with brain tumors

Patient	Cho_n/R	Cho_t/R	NAA_n/R	NAA_t/R	tCr_t/R	L_t/R	Cho_n/NAA_n	Cho_t/NAA_t	WHO Grade
1*	1.08	1.47	2.06	0.86	ND	ND	0.52	1.71	I
2*	0.87	2.53	1.67	0.61	0.25	1.58	0.52	4.15	III
3*	1.07	2.09	1.12	0.57	0.59	4.29	0.96	3.67	III
4*	0.79	1.86	1.13	0.64	0.15	ND	0.70	2.91	IV
5*	0.63	2.68	1.76	0.71	ND	ND	0.36	3.77	I
6*	0.97	1.92	1.71	0.76	0.53	ND	0.57	2.53	I
7*	0.62	1.03	1.22	0.12	ND	ND	0.51	8.58	II
8*	0.88	2.16	1.43	0.22	ND	ND	0.62	9.82	II
9*	1.07	2.17	1.11	1.00	ND	ND	0.96	2.17	III
10*	0.93†	2.20	1.51†	0.12	ND	0.59	0.62	18.33	II
11	0.93	0.99	0.81	0.11	ND	3.81	1.15	9.00	III
12	1.25	0.03	2.23	0.3	0.18	ND	0.56	0.10	IV
13	0.80	0.89	1.67	0.45	0.68	ND	0.48	1.98	IV
14*	0.83	3.17	1.67	0.05	0.37	4.16	0.50	63.4	IV
15*	1.27	1.69	1.54	0.48	1.25	0.67	0.82	3.52	II

Note.—Cho_n indicates mean value of choline in voxels containing only normal tissue as defined in the "Methods" section; R, mean value of the total creatine pool in voxels containing only normal tissue, used as an internal reference; NAA_n, mean value of NAA in voxels containing only normal tissue; tCr_t, mean value of the total creatine pool in voxels containing only abnormal tissue; Cho_t, mean value of choline in voxels containing only abnormal tissue; NAA_t, mean value of NAA in voxels containing only abnormal tissue; L_t, mean value of lactate and lipids in voxels containing only abnormal tissue; ND, not detectable; and WHO, World Health Organization.

* Had biopsy-proved tumors.

† Mean values of normal Cho and NAA from other patients were used since the region of interest contained no voxels of normal tissue.

15 (Figs 1 and 2). In all biopsy-confirmed tumors (patients 1 through 10, 14, and 15), the levels of Cho were substantially increased based on the comparison of the ratio of tumor Cho (Cho_t) to the total creatine pool of normal tissue (R) and the ratio of the Cho of normal tissue (Cho_n) to R (Table 2). The mean value of Cho_t/R for the same tumors, as compared with the mean Cho_n/R, was also significantly increased (Table 3). For patients 11 and 13, the Cho_t/R ratio did not differ from the Cho_n/R ratio. For patient 12, the Cho_t/R ratio was reduced as compared with the Cho_n/R ratio. Furthermore, the level of NAA (patients 1 through 10, 14, and 15) was greatly decreased based on the comparison of the ratio of the tumor NAA (NAA_t) with R and of the ratio of the NAA of normal tissue (NAA_n) with R (Table 2). Also, the mean value of the NAA_t/R as compared with the mean NAA_n/R was significantly decreased in the same patients (Table 3). The level of tCr was decreased in all cases in which it was detected. The ratio of Cho_t to NAA_t was increased in all but one case (patient 12). The mean value of this ratio (patients 1 through 10, 14, and 15) showed a substantial increase from the Cho_n/NAA_n ratio, but this increase was not statistically significant (Table 3).

Radiation treatment led to spectra with lower metabolite peaks (patients 11 through 13, Table 2) and caused a reduction in hemodynamic parameters (patients 6 and 12, Table 1). Areas of residual or suspected recurrent tumor revealed spectra with prominent Cho (patients 5 through 10, Table 2), and hemodynamic MR imaging revealed increased hemodynamics (patients 3 and 14, Table 1).

In three patients, neovascular leakiness was hypothesized by very early enhancement (patients 10 and 13, Table 1). This was confirmed histologically by the presence of very thin-walled vessels (Fig 5). These qualitative observations were enhanced by semiquantitation of hemodynamic MR imaging data in three patients in whom ratios of hemodynamic parameters were calculated. In two patients (patients 1 and 6, Table 1), the hemodynamic parameter ratios of tumor to normal tissue (rCBV, rCBF, and MTT) were 0.21, 0.7, and 0.6, and 0.38, 0.71, and 0.37, respectively. In patient 14 (Table 1), the same parameters were increased (1.37, 1.02, and 1.39).

In most cases we could identify the anaplastic and undifferentiated region of the tumor by a higher intensity region in the Cho image, as shown in Figure 1, corresponding to high Cho levels in the quantitative analysis (Table 2). This was confirmed by histologic studies of the large specimen excised at surgery. This is the highly anaplastic area of the tumor that was

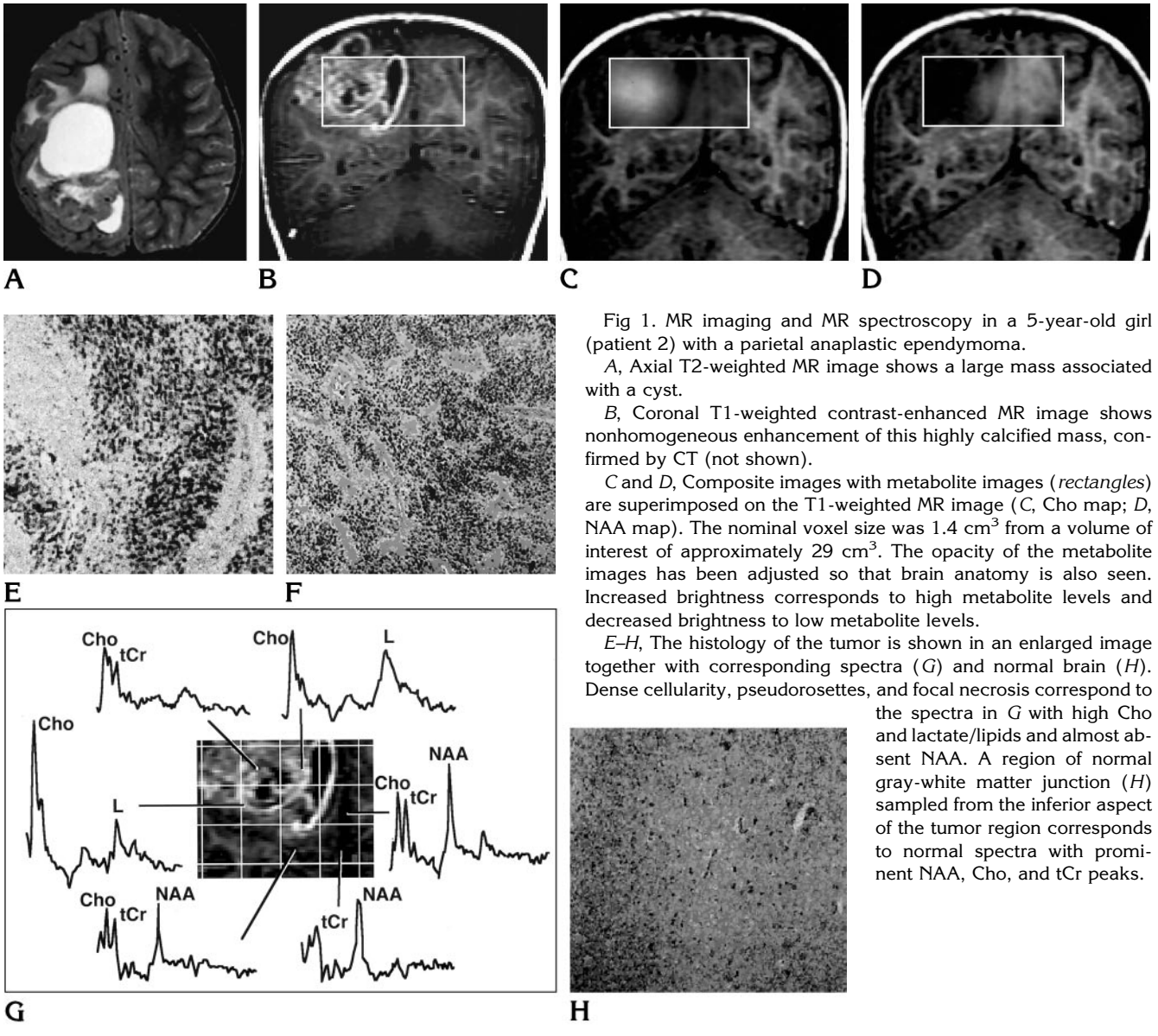

Fig 1. MR imaging and MR spectroscopy in a 5-year-old girl (patient 2) with a parietal anaplastic ependymoma.

A, Axial T2-weighted MR image shows a large mass associated with a cyst.

B, Coronal T1-weighted contrast-enhanced MR image shows nonhomogeneous enhancement of this highly calcified mass, confirmed by CT (not shown).

C and *D*, Composite images with metabolite images (*rectangles*) are superimposed on the T1-weighted MR image (*C*, Cho map; *D*, NAA map). The nominal voxel size was 1.4 cm^3 from a volume of interest of approximately 29 cm^3. The opacity of the metabolite images has been adjusted so that brain anatomy is also seen. Increased brightness corresponds to high metabolite levels and decreased brightness to low metabolite levels.

E–H, The histology of the tumor is shown in an enlarged image together with corresponding spectra (*G*) and normal brain (*H*). Dense cellularity, pseudorosettes, and focal necrosis correspond to the spectra in *G* with high Cho and lactate/lipids and almost absent NAA. A region of normal gray-white matter junction (*H*) sampled from the inferior aspect of the tumor region corresponds to normal spectra with prominent NAA, Cho, and tCr peaks.

classified as an anaplastic ependymoma. The NAA (neuronal marker) was also missing from the region occupied by the tumor.

Discussion

Several studies have suggested the potential of MR spectroscopy to provide independent information regarding brain tumor metabolism and response to treatment (22–28) (P. Luyten, J. den Hollander, C. Segebarth, D. Baleriaux, "Localized 1H NMR Spectroscopy and Spectroscopic Imaging of Human Brain Tumors in Situ," in: *Proceedings of the Society of Magnetic Resonance in Medicine*, Berkeley, Calif: Society of Magnetic Resonance in Medicine; 1988:252; and P. R. Luyten, P. C. van Rijen, L. C. Meiners, J. H. Mariën, J. A. den Hollander, "Identifying Epileptic Foci by ^{1}H NMR Spectroscopic Imaging in Patients with Therapy Resistant Epilepsy," in: *Proceedings of the Society of Magnetic Resonance in Medicine*, Berkeley, Calif: Society of Magnetic Resonance in Medicine; 1990:1009). In children, however, relatively few single-voxel studies (29–31) and, to our knowledge, no chemical-shift imaging studies have been reported. Since brain tumors are heterogeneous, single-voxel MR spectroscopy is unable to assess the spatial distribution of spectral changes accompanying tumor response to treatment

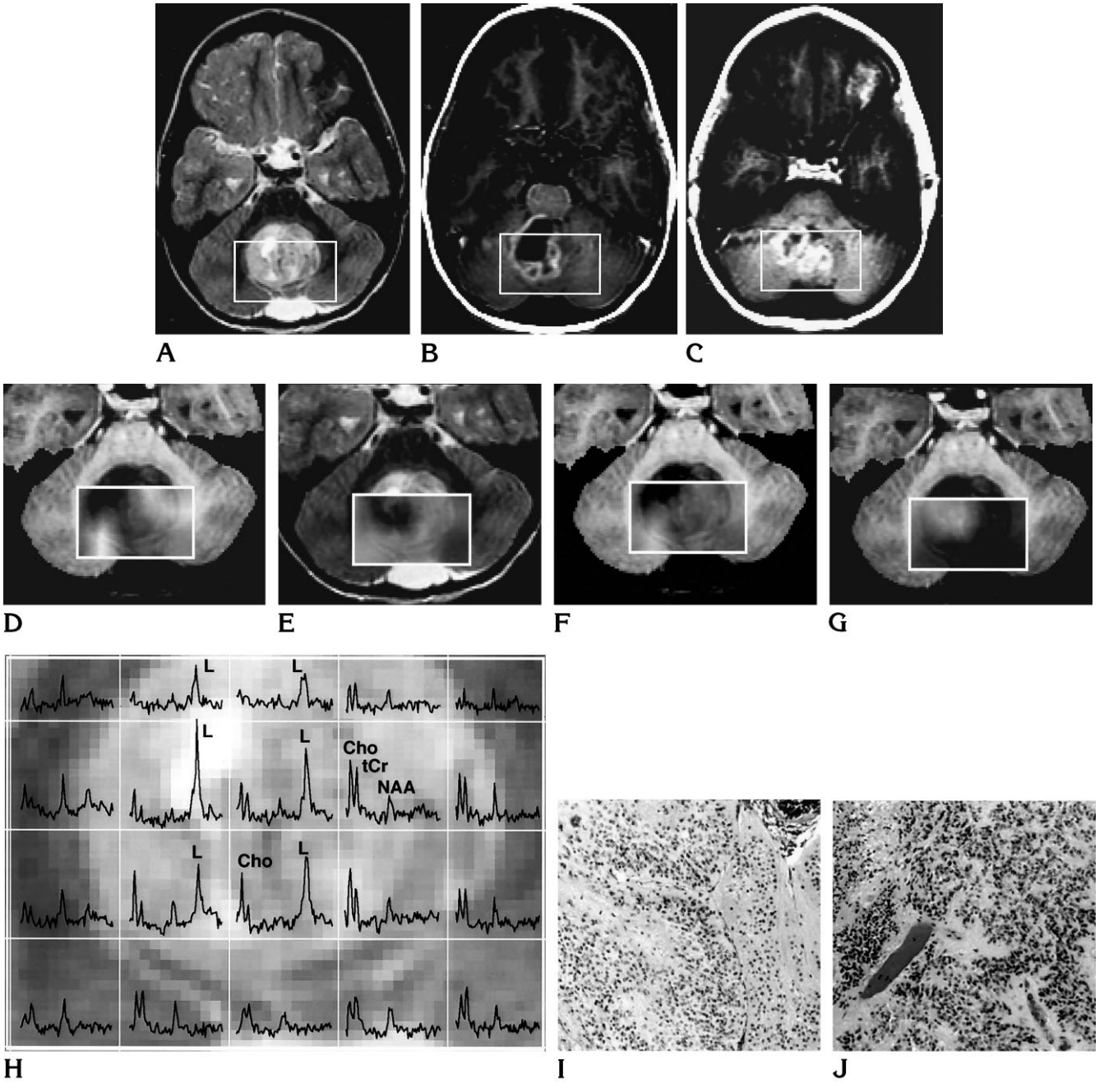

Fig 2. MR imaging and MR spectroscopy in a 4-year-old boy (patient 3) with a large posterior fossa anaplastic ependymoma.

A, Axial T2-weighted MR image shows a large cystic posterior fossa tumor.

B and *C*, Two contiguous axial T1-weighted MR sections after injection of contrast material show a large cyst and nonhomogeneous enhancement. *Rectangles* indicate the volume selected for MR spectroscopy.

D–G, Composite images represent Cho (*D*), NAA (*E*), tCr (*F*), and lactate/lipids (*G*) metabolite distributions (*rectangles*) superimposed on the T2-weighted MR images. Increased brightness corresponds to higher metabolite levels and decreased brightness to lower levels. In *D*, *F*, and *G*, the T2-weighted image contrast has been reversed so that the tumor is dark and does not interfere with the intensity of the metabolite image. Note that the cyst (clearly seen as a dark region in *B*) corresponds to low or no NAA and high lactate/lipids, which suggests that lactic acid has been concentrated in the cyst. *D* shows two regions of high Cho corresponding to the solid portion of the tumor.

H, The spectral grid has been superimposed on a zoomed T2-weighted image. The metabolic heterogeneity of the tumor as depicted by multivoxel MR spectroscopy is illustrated.

I and *J*, Histologic sections show certain regions of the tumor are "typical" ependymoma (*I*), whereas other regions had more anaplastic features, including increased cellularity (*J*).

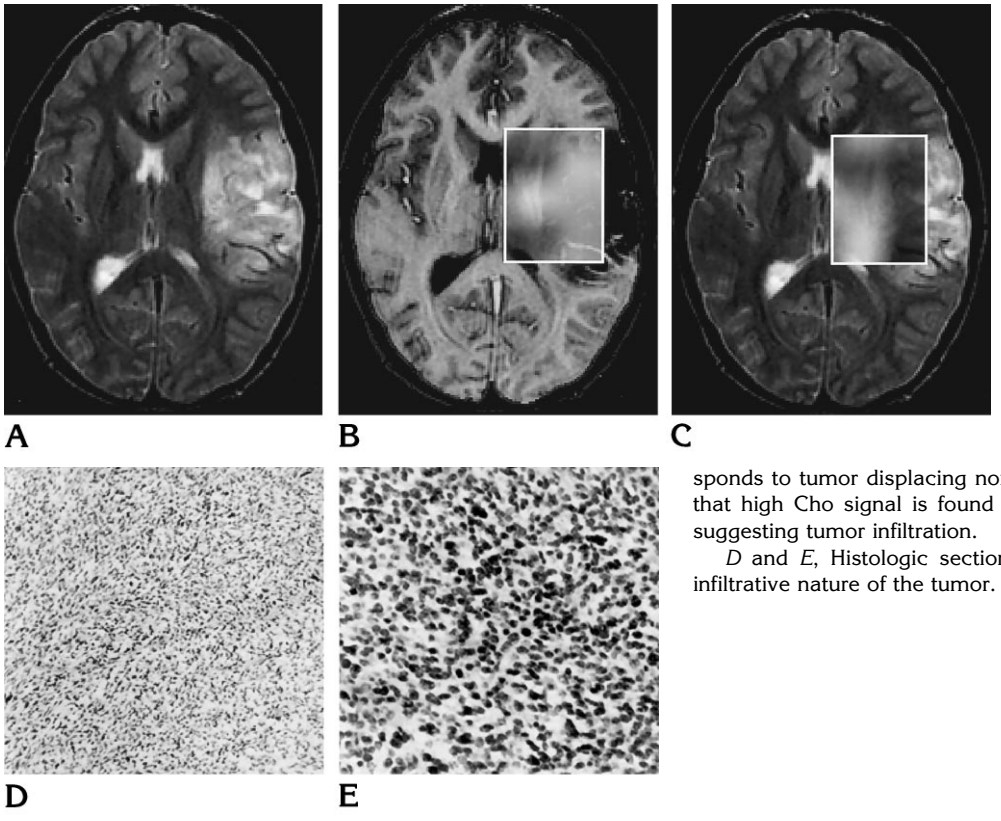

Fig 3. MR and metabolite imaging in a 15-year-old boy (patient 4) with a malignant glial tumor.

A, Axial T2-weighted MR image shows a left-sided frontoparietal lesion.

B, A composite image shows the Cho distribution (*rectangle*) superimposed on the T2-weighted image with reversed contrast.

C, A similarly displayed NAA distribution (*rectangle*) is superimposed on a standard T2-weighted image. The region of very low NAA (dark) corresponds to tumor displacing normal brain tissue. Note, however, that high Cho signal is found where NAA is high (or normal), suggesting tumor infiltration.

D and *E*, Histologic sections show the high cellularity and infiltrative nature of the tumor.

and local control. Knowledge of tumor vascularization is also essential to our understanding of tumor malignancy, since its absence would not permit tumor growth (32). Tumor recruitment of new vessels is a multifactorial process necessary for tumor growth (33, 34). Imaging methods that are sensitive to changes associated with malignant growth include PET and SPECT (2, 3). Recent findings indicate that MR spectroscopy and PET compare well in their ability to detect regions of abnormal metabolism in adult patients with brain tumors (M. Day, D. Vigneron, S. Wald, et al, "Comparison of 3D Proton MR Spectroscopy and F-18 Fluorodeoxyglucose PET for Assessment of Brain Tumor Activity," in: *Proceedings of the Society of Magnetic Resonance and the European Society for Magnetic Resonance in Medicine and Biology*, Nice, France, 1995:544). Nevertheless, the usefulness of PET is limited by its unavailability in most institutions. SPECT, although readily available, does not allow identification of small areas of altered blood volume. Although recent studies in adults suggest that perfusion-sensitive MR imaging can be used for tumor assessment (6, 35), we are not aware of any such data in children.

Our preliminary experience in this study has shown that an MR protocol that gives both multivoxel spectroscopic and hemodynamic data is feasible in the clinical setting (Fig 4). The findings support the hypothesis that active tumor may be differentiated from normal brain tissue and necrosis (Figs 1–3, 5, and 6). These results suggest that serial combined spectroscopic and hemodynamic imaging may be used to monitor the success or failure of tumor control during radiation therapy (Fig 4, patient 6). We propose a hypothesis to assist in distinguishing between normal tissue, recurrent or residual tumor, and necrotic tissue based on the distinctive spectral patterns associated with three different histologic states (Fig 7). These tissue states are also characterized by different hemodynamic patterns. We propose that the combination of spectroscopic and hemodynamic data should enhance the characterization of tumors during the course of treatment (Fig 6). This is because the pathophysiological characteristics of brain tumors with regard to cellularity and vascularity are altered by treatment. MR spectroscopy is sensitive to biochemical changes occurring in neoplasia and provides markers of cellular proliferation. Hemodynamic MR imaging shows the

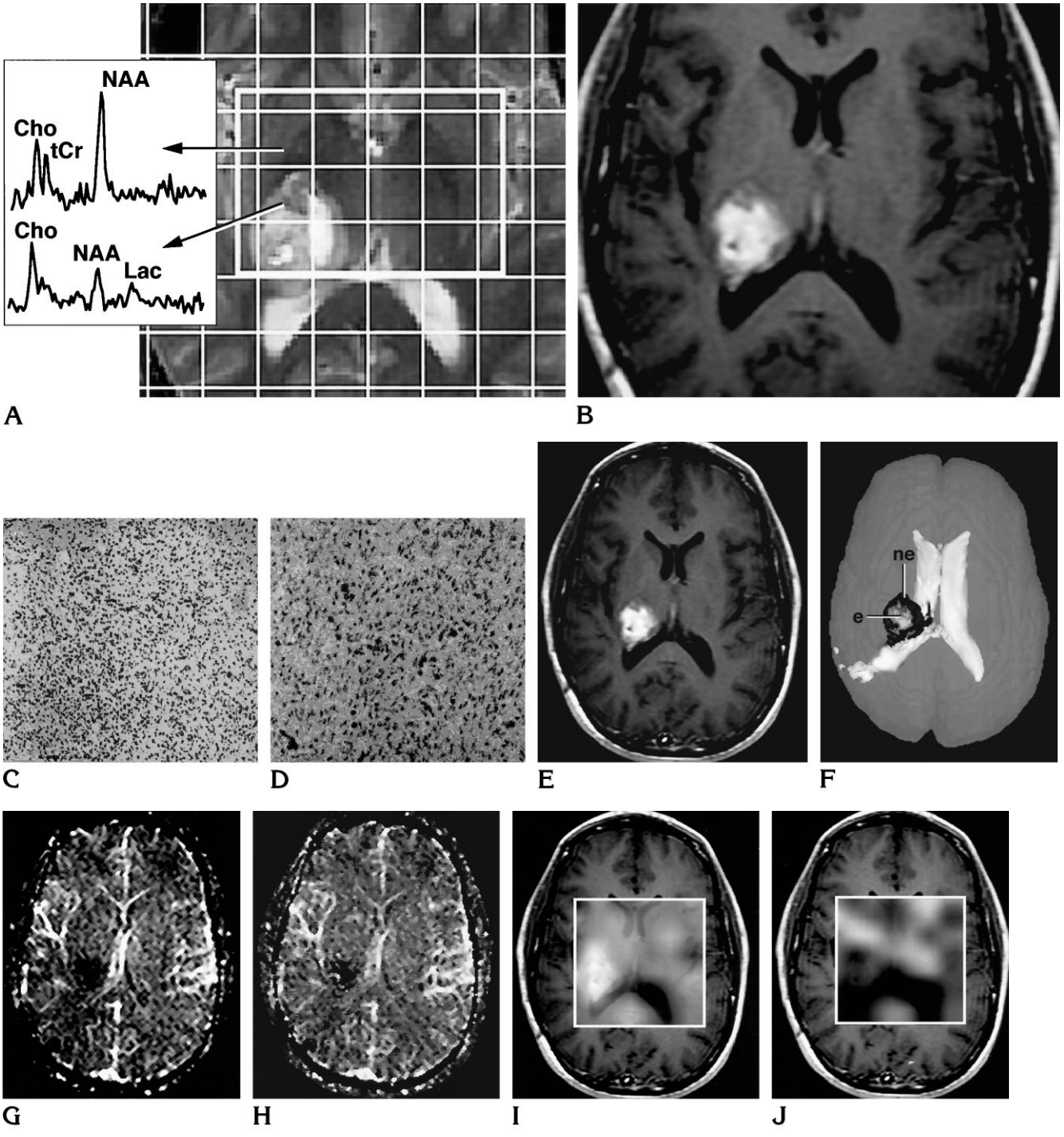

Fig 4. MR and metabolite imaging in a 22-year-old man (patient 6) with a recurrent thalamic fibrillary glial tumor.

A and *B*, Zoomed axial T2-weighted MR image and axial contrast-enhanced T1-weighted MR image, respectively, show an enhancing cystic thalamic mass. *Rectangle* in *A* indicates the region selected for MR spectroscopy. The nominal voxel size was 4.5 cm^3. Two spectra are shown. The upper spectrum exhibits prominent NAA, tCr, and Cho peaks, corresponding to normal tissue. The lower spectrum corresponds to a voxel that contains both tumor and normal tissue and shows a stronger Cho signal, caused by the tumor, and a discernible lactic acid (*Lac*) peak, possibly due to local metabolic acidosis.

C and D, Two magnifications show the characteristic histologic appearance.

E and *F*, Follow-up examination 4 months after stereotactic radiation treatment. Axial contrast-enhanced T1-weighted MR image (*E*) shows the tumor with a smaller cyst. Segmentation (*F*) shows the contrast-enhancing (*e*) and nonenhancing (*ne*) portions of the tumor. The volume of the cyst has been reduced from 20.6 cm^3 to 2.4 cm^3, although *e* (4.5 cm^3) and *ne* (6.8 cm^3) have remained essentially unaltered. *Continues.*

TABLE 3: Comparison of metabolite ratios between tumor regions and normal regions in 12 patients with brain tumors

Group	Cho/R	NAA/R	Cho/NAA
Normal	0.92 ± 0.19	1.49 ± 0.30	0.64 ± 0.19
Tumor	2.08 ± 0.56	0.51 ± 0.32	10.38 ± 17.35
Percentage of difference	126	−66	1522
*P**	.000045	.000005	.079

Note.—Metabolite ratios listed above are derived from patients 1 through 10, 14, and 15 from Tables 1 and 2, since these patients had biopsy-proved tumors. Values presented are the mean ± SD of the ratios. The normal Cho/R, NAA/R, and Cho/NAA values are the mean ± SD of the Cho_n/R, NAA_n/R, and Cho_n/NAA_n values from Table 2. The tumor Cho/R NAA/R and Cho/NAA values are the mean ± SD of the Cho_t/R, NAA_t/R, and Cho_t/NAA_t values from Table 2.

* The *P* values were calculated by means of a paired-variable *t* test.

neovascularization associated with tumor growth. Although the techniques are independent of each other, they complement MR imaging by indicating two additional ways of detecting pathophysiological changes associated with tumor growth.

The characteristics and significance of the three spectral patterns (Fig 7) are discussed below. Normal proton spectra exhibit signals from biologically relevant metabolites such as NAA, tCr, and Cho (36). NAA is believed to be associated with neurons and their processes (37, 38). Creatine and phosphocreatine are compounds involved in energy metabolism and give rise to the tCr signal. Membrane-associated compounds, primarily glycerophosphocholine, phosphocholine, and a small amount of free choline, give rise to the Cho signal in vivo (39). Spectra acquired at shorter echo times contain additional signals from aliphatic groups of lipids and lactic acid (40), which accumulate because of tissue breakdown and metabolic acidosis, respectively.

In our study, childhood brain tumors consistently showed a reduction or absence of both NAA and tCr, attributed to edema and necrosis; an increase in Cho, possibly due to altered membrane metabolism; and an increase in lactate/lipids, probably due to tissue breakdown and metabolic acidosis (Tables 2 and 3; Figs 1–3, and 6). These findings are consistent with the tumor spectral pattern (Fig 7) that is characterized by high Cho, variable tCr, low or no NAA, and variable lactate/lipids. Both single-voxel-localized and multivoxel chemical-shift imaging studies of brain tumors are also in agreement with the hypothesis presented in Figure 7 (25, 27–28, 41–42). Significant reduction of NAA in the brain tumors in this study (Tables 2 and 3) as well as in other studies is expected in tumors of glial origin, since it is primarily localized in neurons. NAA detection within these tumors, therefore, is either due to partial volume averaging with adjacent normal tissue or to tumor infiltration of normal tissue. However, since NAA has been found in cell cultures of oligodendroglia progenitors (43), NAA detection in childhood tumors may also be due to immature oligodendroglia. A reduction in tCr resonance as seen in our data (Table 2) may correspond to exhaustion of energy reserves from rapid cell proliferation and ischemia. It may also indicate cell loss due to necrosis. However, prominent tCr peaks have been observed occasionally in our data sets, partly due to our short-echo protocol (as compared with previous studies). Our data in one case of an infiltrative glioma (patient 15) may also suggest that a prominent tCr peak is due to partial volume averaging with normal brain cells.

The increase in the Cho peak as observed in this study (Tables 2 and 3) is suggested to concur with elevated mobile precursors participating in cell membrane turnover during cell growth (44). If an increase in the Cho peak correlates with increased mitotic and proliferative activity, it may be of prognostic value in assessing the degree of cellular proliferation or response to therapy. Indeed, in this study, the Cho_t/R ratio was close to normal in two patients (patients 11 and 13, Table 1), indicating the effect of treatment, which was confirmed by histologic examination. Furthermore, a necrotic lesion showed absence of any metabolite signals, thus confirming the ability of MR spectroscopy to differentiate active tumor from necrosis (patient 12, Table 1 and Fig 6). Increased levels of Cho have been found in most solid tumors (Figs 1, 3, and 5) except in necrotic high-grade

G and *H*, Calculated MR mapping of relative blood volume (rCBV) (*G*) and blood flow (rCBF) (*H*) show that hemodynamic parameters are reduced in the region of the tumor compared with the contralateral side.

I and *J*, Metabolite distribution maps (*rectangles*) show increased Cho in the tumor region (*I*) and depict absence of NAA in the tumor and ventricles (*J*). This case demonstrates the value of volume MR imaging/MR spectroscopy in providing combined morphologic, hemodynamic, and metabolic assessment in follow-up of pediatric brain tumors.

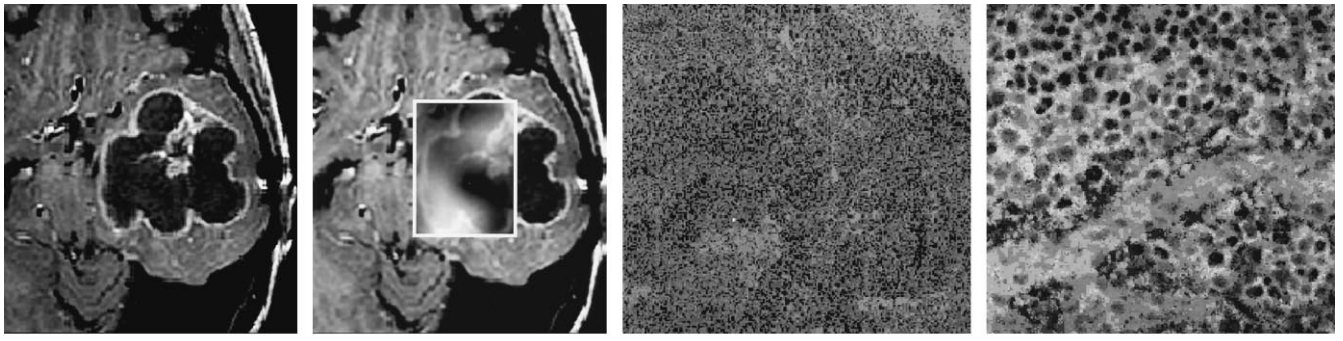

Fig 5. MR imaging and metabolite imaging in an 18-year-old woman (patient 10) with recurrent temporal anaplastic ependymoma.
A, T1-weighted image after administration of contrast material shows an enhancing cystic lesion.
B, Increased Cho on distribution map (*rectangle*) suggests tumor regrowth.
C and *D*, Histologic appearance of the surgical specimen confirms the presence of a highly anaplastic ependymal tumor with pseudorosettes and areas of treatment effect with necrosis. Presence of thin-walled vessels (*D*) correlates with what appeared to be a very "leaky" tumor on MR images (*A*).

tumors, in which the normalized Cho level appears to be decreased (Fig 2, Table 2) (23). In addition, patients with histologically confirmed high-grade tumors (patients 2 through 4, 9, and 14; Table 1) had a large increase in Cho as compared with normal tissue from the same study (Table 2). Even though this suggests that Cho levels may correlate with tumor grade, we did not find any connection between the metabolite ratios and the tumor grade (Table 2). This lack of correlation is probably due to the limited number of patients for each histologic grade. The Cho_t/R ratio (Table 2) may correlate better with histologic grade than any of the ratios derived from single-voxel studies, such as Cho/NAA or Cho/tCr. This speculation is based on the assumption that the Cho_t/R ratio may be a better estimator of the Cho levels in the tumor, since this ratio is not affected by either NAA or tCr of the tumor, both of which have been shown to have variable signal in the tumor spectra. Nevertheless, an increase in the Cho/tCr ratio is reported to correlate with tumor grade (45, 46).

High lactate levels have been attributed to malignant and more aggressive tumors (41, 45, 47). More recent reports dispute the value of lactate as an indicator of malignancy (23, 44). However, the lack of correlation between tumor grade and lactate may be due to discrepancies in biopsy samples and spectra locations (48). Recent findings with high-resolution chemical-shift imaging (which minimizes the tissue heterogeneity problem) and carefully performed histopathologic correlation show that lactate distribution correlates well with density of neoplastic cells in rat gliomas (Y. Luo, B. High, R. de Graaf, M. Terpstra, M. Garwood "Lactate Distribution Correlates with the Density of Neoplastic Cells in Rat Glioma," in: *Proceedings of the Society of Magnetic Resonance and the European Society for Magnetic Resonance in Medicine and Biology*, Nice, France, 1995:65). Other studies indicate that the peaks at 0.9 and 1.2 ppm of the proton spectra may correlate better with malignancy (49–51). In our protocol, lactate cannot be distinguished from lipid. Thus, we evaluate our findings with the assumption that they may both indicate malignancy, especially if we correct for the presence of cyst or necrosis. Detection of lactate and/or lipid peaks in patients 2, 3, 10, 14, and 15 supports the notion that these peaks may indicate malignancy. However this does not hold for other patients in this study. Also, there is no clear correlation between the $lactate_t$/R ratio and tumor grade (Table 2).

Our data confirm the advantages of the multivoxel MR spectroscopic approach to the study of tumors as reported in adult studies (15). Such an approach allows the use of an internal peak standard, namely the tCr peak, for quantitation. This permits evaluation of changes in metabolite levels in the tumor relative to the normal tissue from the same data set (Table 2). Apart from differences between tumor and normal tissue spectra, differences between distinct regions of the neoplastic lesion, such as solid and cystic regions, may also be detected. High

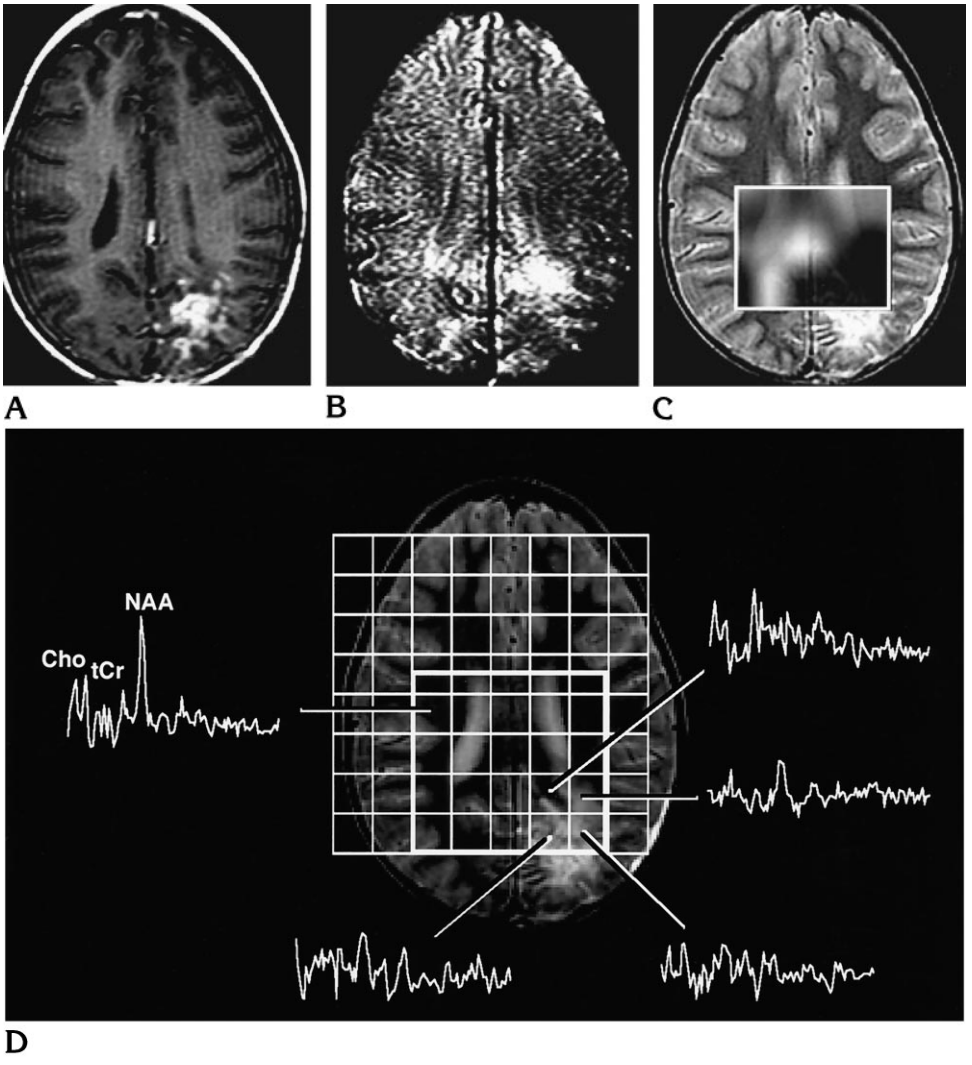

Fig 6. MR and metabolite imaging in a 6-year-old girl (patient 12) treated with radiation therapy and surgery.

A, T1-weighted MR image after injection of contrast material shows enhancement in the location of tumor resection 1 year earlier.

B, Hemodynamic MR image exhibits low perfusion in that region.

C, NAA and Cho images added together and superimposed on the T2-weighted MR image show an absence of these prominent brain metabolites, suggesting tissue necrosis rather than tumor regrowth.

D, Selected spectra are normal or show no metabolite peaks corresponding to the contrast-enhancing region. Histologic analysis confirmed tissue necrosis.

Cho corresponds to solid regions of the lesion, whereas low Cho and NAA coincide with cystic regions (Fig 2). Indeed, cysts exhibit spectra devoid of the metabolites found in normal or tumorous brain regions, except for lactate (27, 28, 31). Also, necrotic centers have been shown to exhibit signals from lactate and lipids (41). After radiation treatment, spectra devoid of signals from metabolites coincide with an absence of tumor cells on histologic evaluation (Fig 6) (22). A more recent proton spectroscopy study in vitro, which included complementary histologic data, supports the notion that proton metabolite levels may characterize gliomas and distinguish tumor from normal and necrotic tissue (52).

The hemodynamic data in this study suggest that increases in hemodynamics coincide with neovascularity, indicating a higher degree of brain neoplasia (patients 3 and 14, Table 1). Decreased hemodynamics are indicative of well-controlled neoplasia, as shown in one representative case (Fig 4G and H). We also hypothesize that necrotic regions have substantially decreased hemodynamics, as demonstrated in another representative case (Fig 6B). These findings are consistent with more elaborative studies in adult patients (6). This information can be used for guiding biopsy by indicating regions with higher degrees of neoplasia. The reason that quantitation was not performed in all patients with tumors was the lack of a blood-brain barrier in neoformated vessels, which leads to early leakage of the contrast agent into the interstitium. Nevertheless, in the limited number of patients in whom quantitation was performed, the information was similar to the qualitative data obtained from

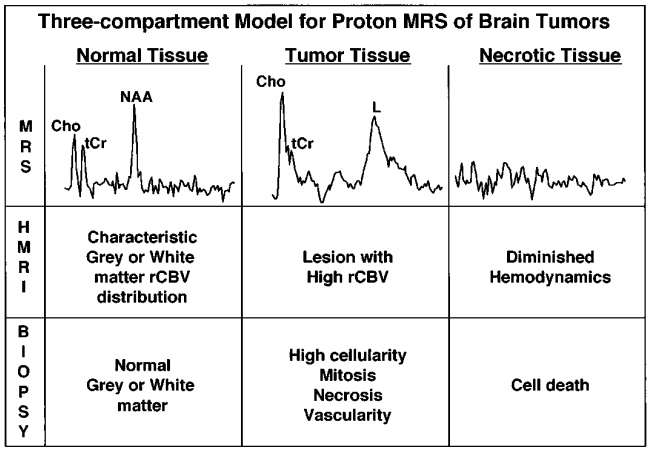

Fig 7. Hypothetical representation of proton MR spectral and hemodynamic patterns of childhood brain tumors. Normal tissue spectra exhibit three prominent peaks: NAA, a neuronal marker; tCr, an energetic status indicator; and Cho, a membrane turnover indicator. Active tumor tissue spectra are characterized by high Cho, variable tCr, and high lactate/lipid peaks, including lactate (metabolic acidosis product) and mobile lipids (degradation products). Necrotic tissue spectra have no metabolite peaks. A combination of these three patterns can be demonstrated by the multivoxel chemical-shift imaging technique. The corresponding hemodynamic MR imaging and histologic patterns are summarized.

other patients. It seems that in patients with tumors in whom leakage through the blood-brain barrier is suspected, an initial bolus of contrast material is necessary to saturate the interstitial space and thus allow quantitation during the second bolus administration.

Hemodynamic parameters, such as rCBV, may be indicators of tumor grade. Although the data presented in this report are not sufficient to prove this thesis, our experience with data of this type supports this notion. The findings of the present study support the hypothesis that active tumor may be differentiated from normal tissue and necrosis on the basis of both spectroscopic and hemodynamic observations. As mentioned earlier, even though these techniques are independent of each other they complement MR imaging and may be indicative of response to treatment. This was apparent in patient 12, in whom both metabolite levels and hemodynamics were abolished because of radiation necrosis effects, which were further confirmed by histologic findings. On the other hand, patient 14, who has been treated with chemotherapy, exhibited both high levels of Cho and hemodynamics consistent with failure of tumor control. These findings were confirmed by histologic examination, which showed the presence of recurrent tumor (Table 1). Similarly, in patient 10, who has been treated with radiation, even though early enhancement prevented the accurate determination of hemodynamics, the Cho level was still an indicator of tumor recurrence, as proved by histologic findings. The Cho level was also an indicator of tumor recurrence in patient 9. Additionally, patients 11 and 13 (Tables 1 and 2), who have been treated with radiation, had regions of signal abnormality on MR images caused either by active tumor or the effects of radiation treatment. In both cases, the Cho level as detected by MR spectroscopy determined that the signal abnormality in these regions resulted from radiation treatment effects, which were subsequently confirmed by histologic examination. In patient 15, although the Cho level suggests that the tumor has been controlled by chemotherapy, follow-up is needed for further confirmation.

In summary, this study verifies that the combination of proton MR spectroscopy and hemodynamic MR imaging provides important data that are unavailable from conventional MR imaging. This metabolic and hemodynamic information allows characterization of childhood brain tumors and their response to therapy.

Acknowledgments

We thank Sarah J. Nelson for assistance with the spectroscopic data processing and critical review of the manuscript and Daniel B. Vigneron for valuable discussions and comments on the MR protocol. In addition, we express gratitude to Peter M. Black, R. Michael Scott, Lilliana Goumnerova, and Nancy Tarbell for patient recruitment and valuable input. Special thanks go to the neuropathologist, Douglas C. Anthony, for providing the photographs of selected histologic slides and helpful suggestions about data interpretation and study design. Thanks also to Amy L. Billet for her help and input, and, finally, we thank Donald R. Kirks for his continuing support and encouragement.

References

1. Ries LAG, Hankey BF, Miller BA, Hartman AM, Edwards BK. *Cancer Statistics Review 1973–88.* Washington, DC: National Institutes of Health; 1991. NIH publication 91–2789
2. Bruggers C, Friedman H, Fuller G, et al. Comparison of serial PET and MRI scans in a pediatric patient with a brainstem glioma. *Med Pediatr Oncol* 1993;21:301–306
3. Kahn D, Follett K, Bushnell D, et al. Diagnosis of recurrent brain tumor: value of ^{201}Tl SPECT vs ^{18}F-fluorodeoxyglucose PET. *AJR Am J Roentgenol* 1994;163:1459–1465
4. Edelman RR, Mattle HP, Atkinson DJ, et al. Cerebral blood flow:

assessment with dynamic contrast-enhanced T2*-weighted MR imaging at 1.5T. *Radiology* 1990;176:211–220
5. Warach S, Li W, Ronthal M, Edelman RR. Acute cerebral ischemia: evaluation with dynamic contrast-enhanced MR imaging and MR angiography. *Radiology* 1992;182:41–47
6. Aronen H, Gazit I, Louis D, et al. Cerebral blood volume maps of gliomas: comparison with tumor grade and histologic findings. *Radiology* 1994;191:41–51
7. Brown TR, Kincaid BM, Ugurbil K. NMR chemical shift imaging in three dimensions. *Proc Natl Acad Sci U S A* 1982;79:3523–3526
8. Maudsley A, Hilal S, Perman W, Simon H. Spatially resolved high resolution spectroscopy by four-dimensional NMR. *J Magn Reson* 1983;51:147–152
9. Bottomley PA, Charles HC, Roemer PB, et al. Human in vivo phosphate metabolite imaging with 31P NMR. *Magn Reson Med* 1988;7:319–336
10. Lenkinski RE, Holland GA, Allman T, et al. Integrated MR imaging and spectroscopy with chemical shift imaging of P-31 at 1.5 T: initial clinical experience. *Radiology* 1988;169:201–206
11. Spielman D, Webb P, Macovski A. Water referencing for spectroscopic imaging. *Magn Reson Med* 1989;12:38–49
12. Vigneron DB, Nelson SJ, Murphy-Boesch J, et al. Chemical shift imaging of human brain: axial, sagittal, and coronal P-31 metabolite images. *Radiology* 1990;177:643–649
13. Taylor JS, Vigneron DB, Murphy-Boesch J, et al. Free magnesium levels in normal human brain and brain tumors: 31P chemical shift imaging measurements at 1.5 T. *Proc Natl Acad Sci U S A* 1991;88:6810–6814
14. Margulis A, Nelson S, Vigneron D. Magnetic resonance spectroscopy. In: *MR '91 Internationales Kerspintomographie Symp Garmish-Patenkirchen*. Constance, Germany: Schetztor-Verlag; 1991
15. Wald L, Moyher S, Day M, Nelson S, Vigneron D. Proton spectroscopic imaging of the human brain using brain phased array detectors. *Magn Reson Med* 1995;34:440–445
16. Belliveau JW, Rosen BR, Kantor HL, et al. Functional cerebral imaging by susceptibility-contrast NMR. *Magn Reson Med* 1990; 14:538–546
17. Villringer A, Rosen BR, Belliveau JW, et al. Dynamic imaging with lanthanide chelates in normal brain: contrast due to magnetic susceptibility effects. *Magn Reson Med* 1988;6:164–174
18. Rempp KA, Brix G, Wenz F, Becker CR, Gückel F, Lorenz WJ. Quantification of regional cerebral blood flow and volume with dynamic susceptibility contrast-enhanced MR imaging. *Radiology* 1994;193:637–641
19. Bottomley PA. Spatial localization in NMR spectroscopy in vivo. *Ann N Y Acad Sci* 1987;508:333–348
20. Nelson S, Brown T. A new method for automatic quantification of 1-D spectra with low signal to noise ratio. *J Magn Reson* 1987; 75:229–243
21. Tzika AA, Massoth RJ, Ball WSJ, Majumdar S, Dunn RS, Kirks DR. Cerebral perfusion in children: detection with dynamic contrast-enhanced T2*-weighted MR images. *Radiology* 1993;187: 449–458
22. van Zijl PC, Moonen CT, Gillen J, et al. Proton magnetic resonance spectroscopy of small lesions (1 ml) localized inside superficial human tumors: a clinical feasibility study. *NMR Biomed* 1990;3: 227–232
23. Fulham MJ, Bizzi A, Dietz MJ, Shih HH, Raman R. Mapping of brain tumor metabolites with proton MR spectroscopic imaging: clinical relevance. *Radiology* 1992;185:675–686
24. Frahm J, Bruhn H, Hänicke W, Merboldt K, Mursch K, Markakis E. Localized proton NMR spectroscopy of brain tumors using short-echo time STEAM sequences. *J Comput Assist Tomogr* 1991;15: 915–922
25. Segebarth CM, Baleriaux DF, Luyten PR, den Hollander JA. Detection of metabolic heterogeneity of human intracranial tumors in vivo by H-1 NMR spectroscopic imaging. *Magn Reson Med* 1990;13:62–76
26. Langkowski JH, Wieland J, Bomsdorf H, et al. Pre-operative localized in vivo proton spectroscopy in cerebral tumors at 4.0 Tesla: first results. *Magn Reson Imaging* 1989;7:547–555
27. Alger J, Frank J, Bizzi A, et al. Metabolism of human gliomas: assessment with H-1 MR spectroscopy and F-18 fluorodeoxyglucose PET. *Radiology* 1990;177:633–641
28. Bruhn H, Frahm J, Gyngell ML, et al. Noninvasive differentiation of tumors with use of localized H-1 MR spectroscopy in vivo: initial experience in patients with cerebral tumors. *Radiology* 1989;172: 541–548
29. Sutton LN, Lenkinski RE, Cohen BH, Packer RJ, Zimmerman R. Localized ^{31}P spectroscopy of large pediatric brain tumors. *J Neurosurg* 1990;72:65–70
30. Sutton L, Wang Z, Gusnard D, et al. Proton magnetic resonance spectroscopy of pediatric brain tumors. *Neurosurgery* 1992;31: 195–202
31. Tzika AA, Vigneron DB, Ball WS, Dunn RS, Kirks DR. Localized proton MR spectroscopy of the brain in children. *J Magn Reson Imaging* 1993;3:719–729
32. Folkman J. Tumor angiogenesis: therapeutic implications. *N Engl J Med* 1971;285:1182
33. Folkman J, Klagsbrun M. Angiogenic factors. *Science* 1987;235: 442–447
34. Folkman J. What is the evidence that tumors are angiogenesis dependent? *J Natl Cancer Inst* 1989;82:4–6
35. Rosen BR, Belliveau JW, Aronen HJ, Hamberg LM, Kwong KK, Fordham JA. Functional neuroimaging. In: Kucharczyk J, Moseley ME, Barkovich AJ, eds. *Magnetic Resonance Neuroimaging*. Boca Raton, Fla: CRC Press; 1994:141–166
36. Hanstock CC, Rothman DL, Prichard JW, Jue T, Shulman RG. Spatially localized ^{1}H NMR spectra of the human brain. *Proc Natl Acad Sci U S A* 1988;85:1821–1825
37. Nadler JV, Cooper JR. N-acetyl-L-aspartic acid content of human neural tumours and bovine peripheral nervous tissues. *J Neurochem* 1972;19:313–319
38. Koller KJ, Zaczek R, Coyle JT. N-Acetyl-aspartyl-glutamate: regional levels in rat brain and the effects of brain lesions as determined by a new HPLC method. *J Neurochem* 1984;43:1136–1142
39. Barker PB, Breiter SN, Soher BJ, et al. Quantitative proton spectroscopy of canine brain: in vivo and in vitro correlations. *Magn Reson Med* 1994;32:157–163
40. Frahm J, Bruhn H, Gyngell ML, Merboldt KD, Hanicke W, Sauter R. Localized high-resolution proton NMR spectroscopy using stimulated echoes: initial applications to human brain in vivo. *Magn Reson Med* 1989;9:79–93
41. Arnold DL, Shoubridge EA, Villemure JG, Feindel W. Proton and phosphorus magnetic resonance spectroscopy of human astrocytomas in vivo: preliminary observations on tumor grading. *NMR Biomed* 1990;3:184–189
42. Luyten P, Marien A, den Hollander J. Acquisition and quantitation in proton spectroscopy. *NMR Biomed* 1991;4:64–69
43. Urenjak J, Williams SR, Gadian DG, Noble M. Specific expression of N-acetylaspartate in neurons, oligodendrocyte-type-2 astrocyte progenitors, and immature oligodendrocytes in vitro. *J Neurochem* 1992;59:55–61

44. Kugel H, Heindel W, Ernestus RI, Bunke J, du Mesnil R, Friedman G. Human brain tumors: spectral patterns detected with localized H-1 MR spectroscopy. *Radiology* 1992;183:701–709
45. Gill SS, Thomas DGT, Van Bruggen N, et al. Proton MR spectroscopy of intracranial tumors: in vivo and in vitro studies. *J Comput Assist Tomogr* 1990;14:497–504
46. Sutton L, Wehrli S, Gennarelli L, et al. High-resolution ^{1}H-magnetic resonance of pediatric posterior fossa tumors in vitro. *J Neurosurg* 1994;81:443–448
47. Radda G, Bore P, Rajagopalan B. Clinical aspects of NMR spectroscopy. *Br Med Bull* 1984;40:155–160
48. Barker P, Glickson J, Bryan R. In vivo magnetic resonance spectroscopy of brain tumors. *Top Magn Reson Imaging* 1993;5:32–45
49. Lazeyras F, Charles HC, Schold C, Fredericks R, Coleman RE. H-1 spectroscopic imaging in gliomas. *J Magn Reson Imaging* 1992;2(Suppl):71–72
50. Ott D, Hennig J, Ernst T. Human brain tumors: assessment with in vivo MR spectroscopy. *Radiology* 1993;186:745–752
51. Posse S, Schuknecht B, Smith M, Van Zijl P, Herschkowitz N, Moonen C. Short echo time proton MR spectroscopic imaging. *J Comput Assist Tomogr* 1993;17:1–14
52. Kinoshita Y, Kajiwara H, Yokota A, Koga Y. Proton magnetic resonance spectroscopy of astrocytic tumors: an in vitro study. *Neurosurgery* 1994;35:606–613